THE JOURNAL OF PHYSICAL CHEMISTRY C
A JOURNAL OF THE AMERICAN CHEMICAL SOCIETY

pubs.acs.org/JPCC
Article

Second-Harmonic Generation in Perovskite Particles for Bioimaging: Unveiling the Effects of Particle Size and Structural Modification

José L. Clabel Huamán,[#] Carlos H. D. Domingues dos Santos,[#] Leonardo De Boni,[#] and Cleber R. Mendonça[#,*]

Cite This: J. Phys. Chem. C 2024, 128, 14801−14810
Read Online

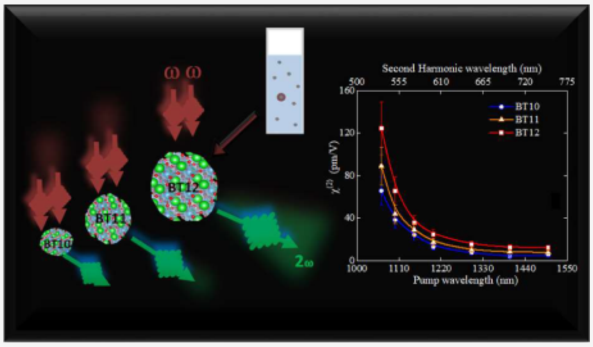

ABSTRACT: Perovskites, particularly $BaTiO_3$ (BT), are renowned for their nonlinear optical applications, notably second harmonic generation (SHG). This study investigates the interplay among the particle size effect, lattice distortion, and electron−phonon coupling, focusing on their collective impact on the second-order nonlinear optical susceptibility ($\chi^{(2)}$) of $BaTiO_3$. BT particles of varying sizes were synthesized using the solid-state reaction method and subsequently subjected to different thermal treatments. Using Raman spectroscopy and X-ray diffraction, the SHG response's intrinsic relationship with $\chi^{(2)}$ was analyzed concerning lattice parameters, particle size, and other pivotal factors. The Raman modes show a systematic blueshift of the phonon mode ($\Delta\omega = 15\ cm^{-1}$) and asymmetrically broadened Raman lines, understood in terms of the lattice strain associated with the particle size effect induced by thermal treatment. A correlation was identified between lattice distortion and SHG response. The increase of the tetragonality ratio, associated with shifts in the Ti−O bond length, correlated with net dipole moments spanning from 1.9×10^{-31} to 2.5×10^{-31} C m and significantly influenced $\chi^{(2)}$ values. Besides, the spectroscopy studies showed that Mie resonances can enhance the conversion efficiency of SHG approximately 2.4 times. At last, the improved SHG in modified BT particles, with higher $\chi^{(2)}$ and biocompatibility, shows potential for high-resolution, low-interference bioimaging applications. The findings highlight the feasibility of optimizing $BaTiO_3$ perovskite materials' nonlinear optical properties by adjusting the particle size and lattice structures, providing beneficial insights for advanced optical and medical imaging applications.

1. INTRODUCTION

Ferroelectric materials, especially at the micro- and nanoscale, have gained significant attention due to their nonlinear optical (NLO) harmonic generation capabilities.[1,2] These properties are essential in photonics research and have potential applications in innovative sensing and imaging techniques across materials science and chemistry.[3−5] One of the key processes in nonlinear optics is the second harmonic generation (SHG), in which, from a quantum mechanics point of view, two photons at a frequency (ω) are annihilated and one photon at double the fundamental frequency (2ω) is created.

Perovskite particles, such as $BaTiO_3$, are a focal point in this domain.[6,7] Their noncentrosymmetric crystal structure at both micro- and nanoscales gives them distinct properties. Recent studies highlighted a robust SHG enhancement in structures using $BaTiO_3$, setting them apart from materials like $LiNbO_3$ and $KNbO_3$.[8−10] While these latter materials are recognized for their NLO responses, they present limitations in conversion efficiency.[11] Compared with pure metallic nanostructures, which face challenges like high visible range losses and intricate fabrication,[12] $BaTiO_3$ particles stand out. Also, $BaTiO_3$ sizes offer a more significant noncentrosymmetric material volume, potentially improving the SHG response. Their SHG process, even on the microscale, makes them prime candidates for diverse nonlinear optical applications.

For $BaTiO_3$, while the influences of size and shape on SHG efficiency are well-charted, the lattice structure distortion, especially its tetragonality, assumes a significant role. These distortions and changes in electronic and photonic states could magnify SHG. Micron-sized particles bring these intricacies to the forefront, where surface-to-volume ratios majorly steer optical behaviors. Although numerous studies use incoherent second-harmonic to probe inorganic and metallic particles' hyperpolarizability,[13−15] understanding the optical second-

Received: May 8, 2024
Revised: July 11, 2024
Accepted: July 12, 2024
Published: August 23, 2024

https://doi.org/10.1021/acs.jpcc.4c03049

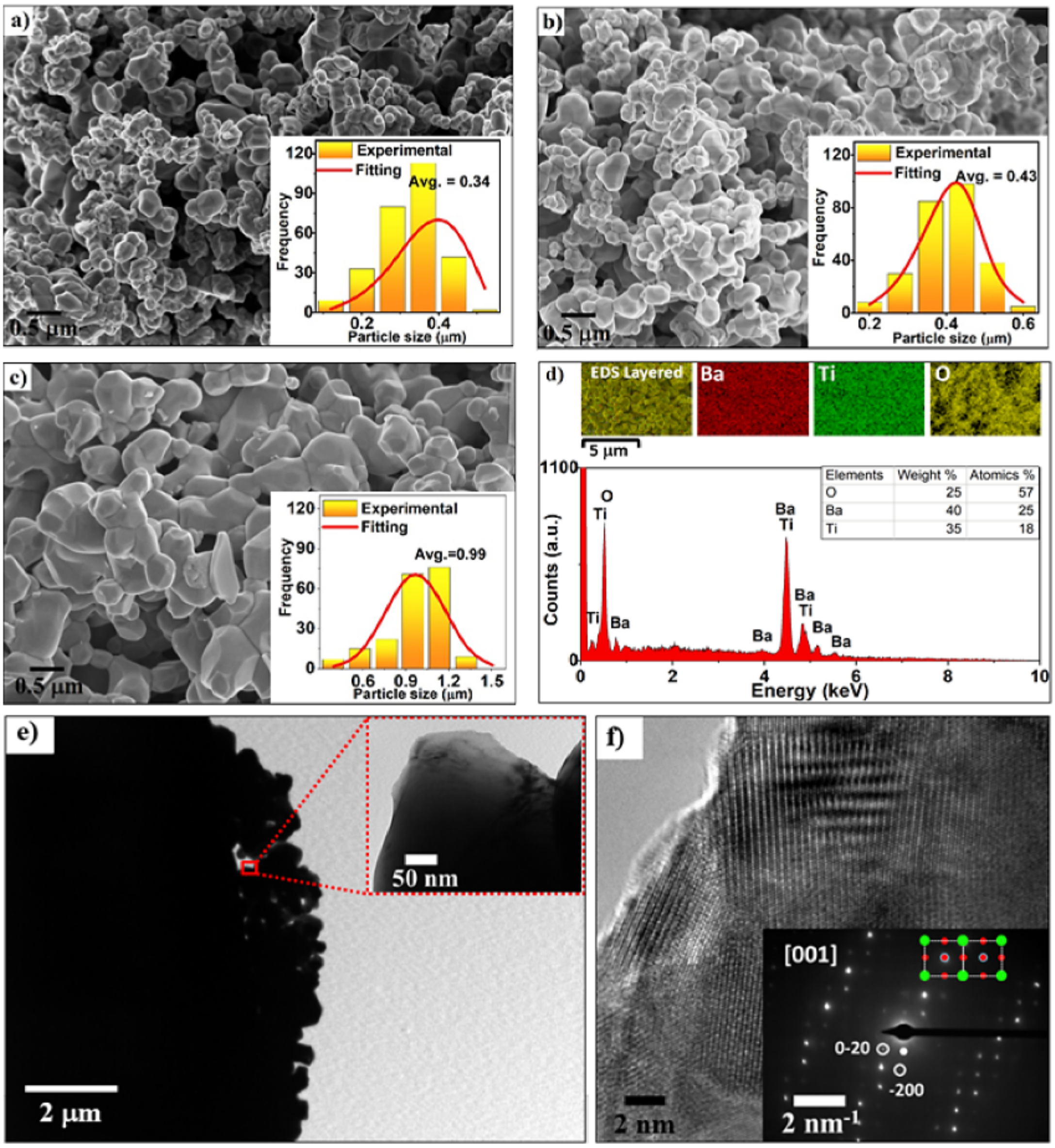

Elements	Weight %	Atomics %
O	25	57
Ba	40	25
Ti	35	18

Figure 1. (a−c) SEM images (5 × 5 μm^2); the insets are the corresponding histograms to particle size for the BT10, BT11, and BT12 samples, respectively. (d) Overlay of various elements on the image (EDS layered) and energy-dispersive X-ray (EDX) spectrometry element-mapping images of BT12 powder ceramics for Ba (red), Ti (green), andO (yellow). (e) TEM image of BT12 powder ceramics; the inset is the corresponding magnification. (f) High-resolution TEM image; the inset shows the SAED patterns of the perovskite phase along the [001] zone axis.

order response, especially concerning lattice distortions in perovskite particles, is still in its early stages, in both computational and experimental cases.

The exceptional SHG properties of $BaTiO_3$ are particularly promising for advanced bioimaging. Their enhanced efficiency and biocompatibility enable high-resolution, low-interference imaging, which is crucial in biomedical research and diagnostics.[16−18] This underscores the importance of studying the $BaTiO_3$ particle size and lattice structure in SHG applications.

This study endeavors to fill this knowledge void, the size particle effect, and understand the lattice structure distortion on the magnitude of SHG. Therefore, this work aims to quantify $\chi^{(2)}$ for particles, deepening the comprehension of perovskite particles' physical chemistry and its influence on the optical nonlinearities.

2. METHODS

Barium titanate powder (abbreviated as BT) was synthesized using the conventional solid-state reaction method (SSRM).[19] High-purity $BaCO_3$ (99.98%) and TiO_2 (≥99%) powders, purchased from Sigma-Aldrich, were used as precursors. Stoichiometric quantities of the precursor materials were ball milled for 12 and 2 h in 2-propanol, purchased from Synth, using zirconium oxide balls (0.5 mm) as the milling medium. After drying, these thoroughly mixed powders were calcined at 1000, 1100, and 1200 °C for 2 h in closed alumina crucibles to verify the effect of calcination on the particle size and the crystalline phase of the $BaTiO_3$. The samples calcined at 1000, 1100, and 1200 °C for 2 h were labeled BT10, BT11, and BT12, respectively.

The crystallinity and phase structure of the BT ceramic powders were investigated by X-ray diffraction (XRD) using a

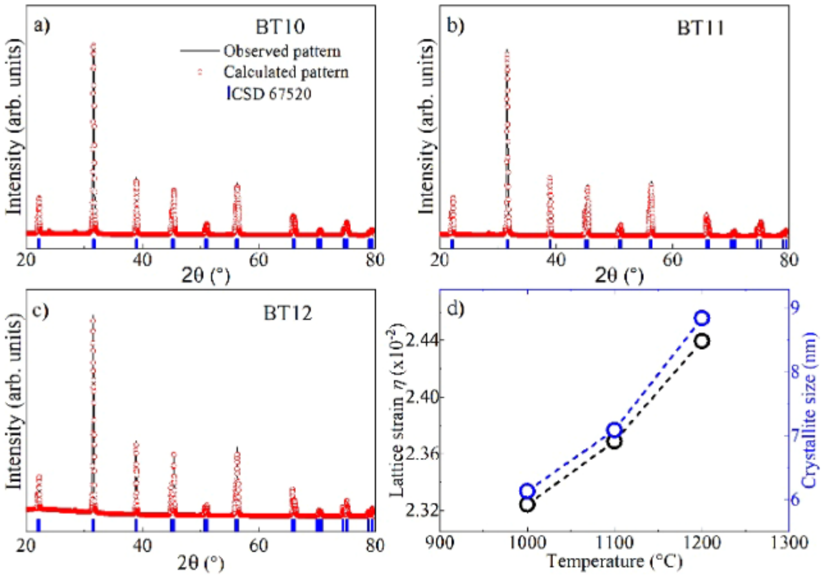

Figure 2. Rietveld plots, from 44° to 46° in 2θ, for different $BaTiO_3$ samples, after thermal treatment: (a) 1000 °C, (b) 1100 °C, and (c) 1200 °C. (d) Lattice strain and crystalline size as a function of temperature.

Rigaku Ultima IV instrument, model Ultima IV (with Cu Kα radiation), in an angular range from 5° to 110° at a scanning rate of 5° min^{-1} and a step size of 0.02°/s, for the BT ceramic powders and thermally treated postmilling. Rietveld refinement was employed to obtain detailed structural information on the BT ceramic powders.

The surface morphology of the BT ceramic powders was characterized by using a field emission gun scanning electron microscope (FEG-SEM), Zeiss Sigma (Germany) model, operating at 15 kV. Chemical analysis by energy-dispersive X-ray spectroscopy (EDS) (Quantax EDS-Bruker) coupled to a scanning electron microscope (TM3000-Hitachi) was also performed. Selected area electron diffraction (SAED) and HRTEM measurements were carried out using a Phillips CM 200 operating at an accelerating voltage of 200 kV with a LaB6 filament. The HR-TEM and SAED images were processed using the CrysTBox software.[20]

Raman spectroscopic studies were performed on a confocal Raman microscope (Witec-ALPHA-300R) with a diode laser at 785 nm, focused on the sample using a 100× objective to measure micro-Raman spectra in backscattering geometry. The recorded Raman spectra of all samples were fitted by the superposition of Lorentzian functions.

The SHG measurements were obtained by the femtosecond-tunable hyper-Rayleigh scattering (HRS) technique. The optical setup consists of an optical parametric amplifier (Orpheus—Light Conversion), pumped by an amplified femtosecond laser system (Pharos—Light Conversion, 1030 nm, 190 fs, 7.5 kHz), as tunable laser excitation, allowing measurements from 1064 to 1500 nm to determine the dispersion of SHG of BT samples. The signal of $I(2\omega)$ versus $I(\omega)$ is collected by a nanosecond photomultiplier and a solid-state photodetector (Si or Ge). More details of the experimental optical setup and the methodology can be found in ref[21].

3. RESULTS AND DISCUSSION

3.1. Structural and Microstructural Analysis.

The scanning electron microscope (SEM) images, shown in Figure 1, represent the morphology of the BT ceramic powders calcinated at different temperatures, called here as BT10 (a), for 1000 °C; BT11 (b), for 1100 °C; and finally BT12 (c), for 1200 °C. The SEM analysis pointed out that the structure of calcinated particles shows homogeneous shapes and monomodal distribution, as shown in the inset of Figure 1a−c. Here, the effect of temperature and milling time plays a key role in the size control of lattice defects, including dislocations and vacancies.[22,23] After an increase in temperature treatment, the average particle size increased from 0.34 to 0.43 μm and to 0.99 μm in the samples BT10, BT11, and BT12, respectively. The corresponding standard deviations of 0.06, 0.09, and 0.21 indicate low to moderate dispersion around the mean, which is typical in many particle size distributions. In addition, all elements of BT12 ceramic powder have also been confirmed to be evenly distributed by the element-mapping analysis, as shown in Figure 1d, indicating a high chemical uniformity in this system.

Based on the described analysis, subsequent TEM, HR-TEM, and SAED measurements were carried out. In Figure 1e, the TEM image shows the formation of homogeneous shape particles, also observed in the high-magnification TEM images; see the inset of Figure 1e. High-resolution transmission electron microscopy (HR-TEM) images prove that these powder ceramics have high crystallinity and narrow size distribution. The crystalline interplanar spacing of about 2.2 Å was obtained directly from the inverse fast Fourier transform images, as shown in the inset of Figure 1f. The SAED pattern (see the inset of Figure 1f) further confirms the tetragonal phase structure in BT12, and the intense diffraction reveals that it corresponds to (0 −2 0) and (−2 0 0) planes in the [001] direction (ICSD no. 67520).[24]

The X-ray diffraction (XRD) patterns in Figure 2 were further analyzed by using the Rietveld refinement method based on EDS analysis. The obtained Rietveld XRD patterns confirm the tetragonal phase of BT10, BT11, and BT12, which agrees with ICSD database N° 67520, with the space group $P4mm$ without any impurities. Table 1 presents the crystalline structure parameters, fit quality (χ^2), and R factors (R_{wp}, R_p, and R_{Bragg}) resulting from the refinement procedure. The

Table 1. Refined Lattice Parameters and Respective Agreement Factors for Each Refinement

samples	BT10	BT11	BT12
space group		*P4mm*	
volume (Å^3)	64.3721 (0.0014)	64.3407 (0.0014)	64.328 (0.0017)
a (Å)	3.99840 (6)	3.99598 (6)	3.99425 (8)
b (Å)	3.99840 (6)	3.99598 (6)	3.99425 (8)
c (Å)	4.02648 (8)	4.02939 (8)	4.03209 (8)
R_{wp} (%)	11.35	13.985	11.397
R_{Exp} (%)	2.64	3.01	2.99
x^2	4.29	4.64	3.80

Rietveld plots closely match theoretical and observed XRD patterns, with the fit quality being supported by the obtained *R* factors.

A temperature increase in thermal treatment results in diffraction peaks that are lower and broader, suggesting a growth in the average crystalline size from 6.3 to 8.8 nm, which indicates that the crystalline size of the BT particles is modulated by thermal treatment. The tetragonality (c/a) for BT10 (1.0069) and BT11 (1.0083) is lower than that of BT12 (1.0096). These tetragonal lattice parameters align well with values published by Hasbullah et al.[25] The variation in values for BT10 and BT11 compared to BT12 could be attributed to size effects and lattice strain.[26] Thermal treatment influences both the crystallite size and the crystallographic parameters. The microstructural analysis revealed that the particle size expands with minimal agglomeration at elevated temperatures. Thus, temperature not only governs nucleation but also affects the growth and size of the BT particles. The latter is also influenced by milling time, which is consistent with the literature.[22]

The $BaTiO_3$ structure comprises O^{2-} anions and Ti^{4+} charge-balancing counter cations. This coordination causes distortion, mainly due to the slight displacement of O^{2-} ions relative to the Ba^{2+} and Ti^{4+} ions. Specifically in BT12, the Ti−O_{axial} bond length (2.0160(5) Å) is longer than the Ti−$O_{equatorial}$ bond length (1.9971(5) Å), which is comparable to the average Ti−O_{axial} bond length of 2.0177 Å reported in the literature.[27] This structural variation, driven by an optimized Ti−O bond alignment along with the density of the TiO_6 octahedron, contributes to the significant increase in the SHG efficiency of $BaTiO_3$, which will be discussed later.

In the BT structure, changes in lattice parameters or unit cell volume depend on cation distribution, chemical composition, and doping.[28] Although thermal treatment does not significantly modify the cationic balance, it does influence the particle size and average crystallite size, as confirmed by SEM, EDS, and HR-TEM analyses. These variations are likely linked to local defects and lattice strain, as suggested in recent studies.[29,30] According to the reported literature,[31] the significant interplanar spacing change can be caused by heat treatment.

3.2. Raman Spectroscopy.

Figure 3a displays the Raman spectra of the BT particles annealed at different temperatures. Interestingly, no spectral differences are observed with an increase in temperature. Typically, the Raman spectrum of BT particles is divided into three sections corresponding to the energy of phonon modes: Ba−O bond, Ti−O bond, and TiO_6 octahedral vibration. The band at ~193 cm^{-1} is attributed to the $A_1(TO_1)$ mode, corresponding to the ferroelectric soft phonon mode.[32] The symmetric $A_1(TO_2)$ modes at 271 cm^{-1} are associated with the characteristic peak for the tetragonal phase with Ti−O stretching. The asymmetric mode A_1(TO) at ~522 cm^{-1} arises from O−Ti−O symmetric stretching. The presence of the A_1(TO) modes has been considered an evidence of a polar instability in the system due to variation d(Ti−O) of the TiO_6 octahedral around c-axes.[33] Furthermore, the peaks at 313 cm^{-1} [B_1 + E(TO + LO)] and 720 cm^{-1} [E(LO) + A_1(LO)] are associated with the structural tetragonal change within the TiO_6 octahedron and phonons propagating along the c-axis of the lattice, respectively. The split of the transverse and the longitudinal optic modes confirms the tetragonal phase with *P4mm* symmetry, consistent with the XRD results.

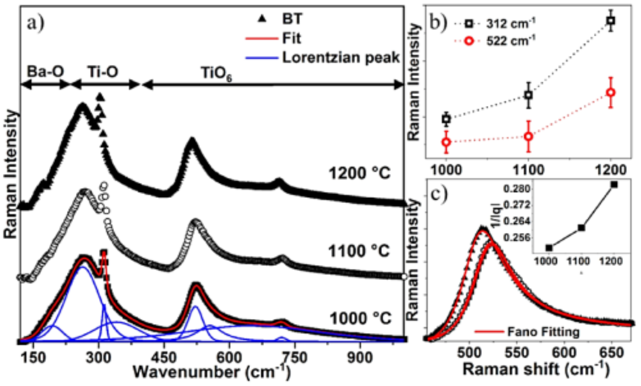

Figure 3. (a) Raman spectra on different calcination temperatures of BT, (b) shift Raman dependence on the temperature at 312 and 522 cm^{-1}, and (c) Fano line shape corresponding to the asymmetric mode A1(TO) for BT samples. The symbols represent the experimental data, and the red lines are the Fano profile fits. The inset represents the temperature dependence of $1/|q|$.

Several factors, such as structural disorder (dangling bonds, lattice strain), broadening due to size distribution, chemical defects (such as oxygen vacancies), particle size, and phonon confinement, can all contribute to the subtle changes in the features of the Raman spectra.[34] The particle size variation affected the Raman peak position and fwhm.[35] At this point, it is worth mentioning that increasing and narrowing of the phonon mode was observed with the particle size increase (see Figure 3b). The blueshift of phonon mode ($\Delta\omega$ = 15 cm^{-1}), see Figure 3c, can be explained as a consequence of the lattice strain associated with the particle size effect, induced by the increase of temperature from 1000 to 1200 °C.[35] Chandramohan et al.,[36] from the application of the phonon confinement model, have shown that $\Delta\omega$ is lower for a particle size higher than 150 nm. Peak broadening and blueshift of the modes' phonons with the increase of temperature has also been shown by Sati et al.[37]

The scattering from the asymmetric profile of the TO_4 mode was observed at ~519 cm^{-1}. Such scattering suggested coherent interference between the discrete phonon and a broad peak.[38] To obtain information from TO_4 mode, fitting using the Fano equation was applied:

$$I(\omega) = I_c \frac{|q - \varepsilon|^2}{1 - \varepsilon^2} + I_b(\omega)$$

where $\varepsilon = (\omega - \omega_0)/\Gamma$ is the reduced frequency and I_c is the amplitude. ω_0 and Γ are the renormalized phonon frequency and the full width at half-maximum of the Fano resonance in the Raman spectrum, respectively. q is the Fano asymmetry parameter that arises from the interaction of a localized discrete state (or discrete phonon) coupled to the continuum states, which determines the line shape of the Fano resonance.[38] The quantity $1/|q|$ is proportional to electron–phonon coupling. The fitting using the Fano function of the TO_4 mode in the phonon frequency at 522 cm^{-1} is shown in Figure 3c as the red lines. The $1/|q|$ of the TO_4 mode was also obtained as a function of temperature (see the inset in Figure 1c). The asymmetric behavior reflects the presence of polarization fluctuations within localized regions. It can arise likely from surface-active sites on the particle surface and defects, such as oxygen vacancy. Increasing the temperature, q showed a decrease in magnitude, suggesting a high electron–phonon coupling. This can be understood as follows: as the temperature increases, the presence of the surface-active site and oxygen vacancy decreases, and the local lattice distortions of the d(Ti–O) octahedron around the c-axes over a particular space are enlarged (see Table 1), leading to a long-range stability. Such long-range stability explains the change in the q asymmetry values. Previous reports show a similar trend is observed in doped $SrTiO_3$ and $KTaO_3$ at room temperatures and is attributed to Fano resonance.[39,40] Sendova et al.[41] have stated that the long-range stability of the Ti–O bond strength is the size-dependent effect. This spectroscopic evidence agrees with X-ray diffraction data of tetragonality reduction with particle size.

Building on the observed structural parameters, Raman spectroscopy, and electron microscopy, which highlighted significant changes in tetragonality and bond configurations, we delve into the microscopic mechanisms that underpin these structural impacts on the nonlinear optical properties of $BaTiO_3$. At the microscopic level, the increase in tetragonality within $BaTiO_3$ nanoparticles influences the electron distribution and polarization behaviors crucial for enhancing nonlinear optical properties.[42,43] Tetragonal distortion in the perovskite structure results in an asymmetric arrangement of atoms within the unit cell, particularly affecting the positions of the Ti and O atoms. This asymmetry alters the electronic polarizability by inducing a noncentrosymmetric polarization distribution, which is essential for SHG. The detailed insights provided by electron microscopy and Raman spectroscopy reveal that with increased tetragonality, there is a notable shift in the Ti–O bond lengths, contributing to a more pronounced polar behavior in the material. These changes at the atomic level affect the local electronic environment, enhancing the material's ability to polarize in response to an electric field, thereby increasing the $\chi^{(2)}$ values. This direct link between the lattice structure and electronic properties highlights the critical role of crystallographic modifications in optimizing the nonlinear optical response of $BaTiO_3$ nanoparticles.

3.3. SHG Measurements of $BaTiO_3$ Particles. The schematic representation of the BT particle from ceramic powders and its inherent tetragonal structure is depicted in Figure 4a. Figure 4b provides a simplified schematic overview of the experimental setup for SHG measurements, emphasizing the flexibility introduced by evaluating varied particle sizes.[21] Using an fs-pulse duration laser for our measurements mitigates the thermal effects seen with an ns-pulse duration laser, ensuring more accurate SHG observations.

After our SHG measurement approach is summarized, it is important to clarify a key aspect of our experimental analysis. While the manuscript references $\chi^{(2)}$ in the context of second-order nonlinear optical susceptibility, it is critical to note that our experiments do not directly measure $\chi^{(2)}$. Instead, we measure the hyperpolarizability of the $BaTiO_3$ particles, which is then normalized by volume to calculate $\chi^{(2)}$. This step is essential for correctly comparing bulk material properties and accurately assessing how the particle size and lattice structure impact SHG efficiency.

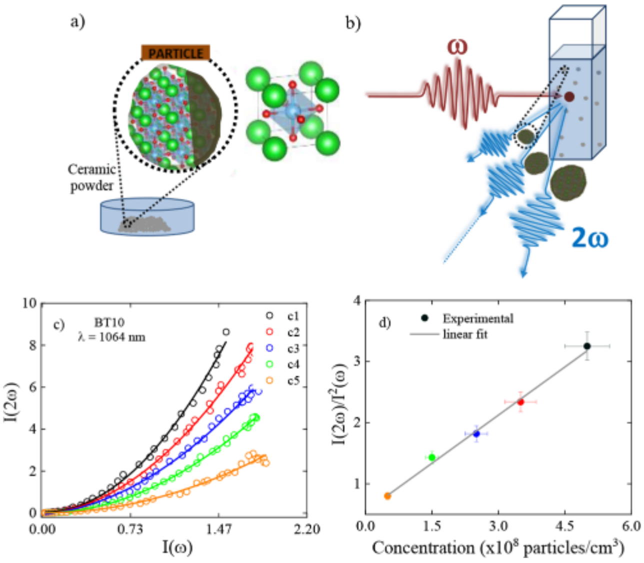

Figure 4. (a) Schematic representation of ceramic powders and their tetragonal structure correspondence. TiO_6 octahedra are drawn in blue, and barium, titanium, and oxygen atoms are represented with green, blue, and red circles, respectively. (b) Schematic representation of the experimental setup showing the SH signal for particles' size difference. (c) Quadratic dependence of SH signals for pump intensity for BT10 at λ = 1064 nm, where c1 is the most concentrated sample. (d) Quadratic coefficient as a function of concentration for Figure 4c. Concentrations are around units of 10^8 particles/cm^3.

The particle size of $BaTiO_3$ directly impacts nonlinear responses. A bulk-like behavior predominates for sizes above 100 nm, and quantum confinement effects can be neglected.[44] Notably, in noncentrosymmetric media, when the particle size is on the order of the pump wavelength, the NLO process, like second harmonic scattering (SHS) or SHG, can emerge, as suggested by Roke and Gonella.[45] The BT10 sample showed consistent $I(2\omega)$ versus $I(\omega)$ signals across both vertical (I_V) and horizontal (I_H) detection polarizations. Therefore, this evidence suggests a SHG process for all studied particles. After determining the origin of the second harmonic signal, dispersion measurements were conducted using wavelengths from 1064 to 1500 nm. As shown in Figure 4c, for a wavelength at 1064 nm, the I(2ω) intensity increases quadratically with pump intensity ($I(\omega)$), consistent with the expectations for a second-order nonlinear process. The quadratic coefficients $I(2\omega)/I^2(\omega)$ as a function of the particle concentration show linear behavior expected for this measurement (see Figure 4d).

SHG dispersion measurements show that all samples have a high value of $\chi^{(2)}$ at λ_{pump} = 1064 nm (Figure 5a). This significant uptick toward shorter wavelengths can be attributed to the enhancement of the Mie resonance process as demonstrated by Timpu et al.[46] In the Mie resonances, most of the confinement of the electromagnetic field occurs inside the dielectric nanostructure and is not constant due to its size, leading to the generation of multiple modes, i.e., is an

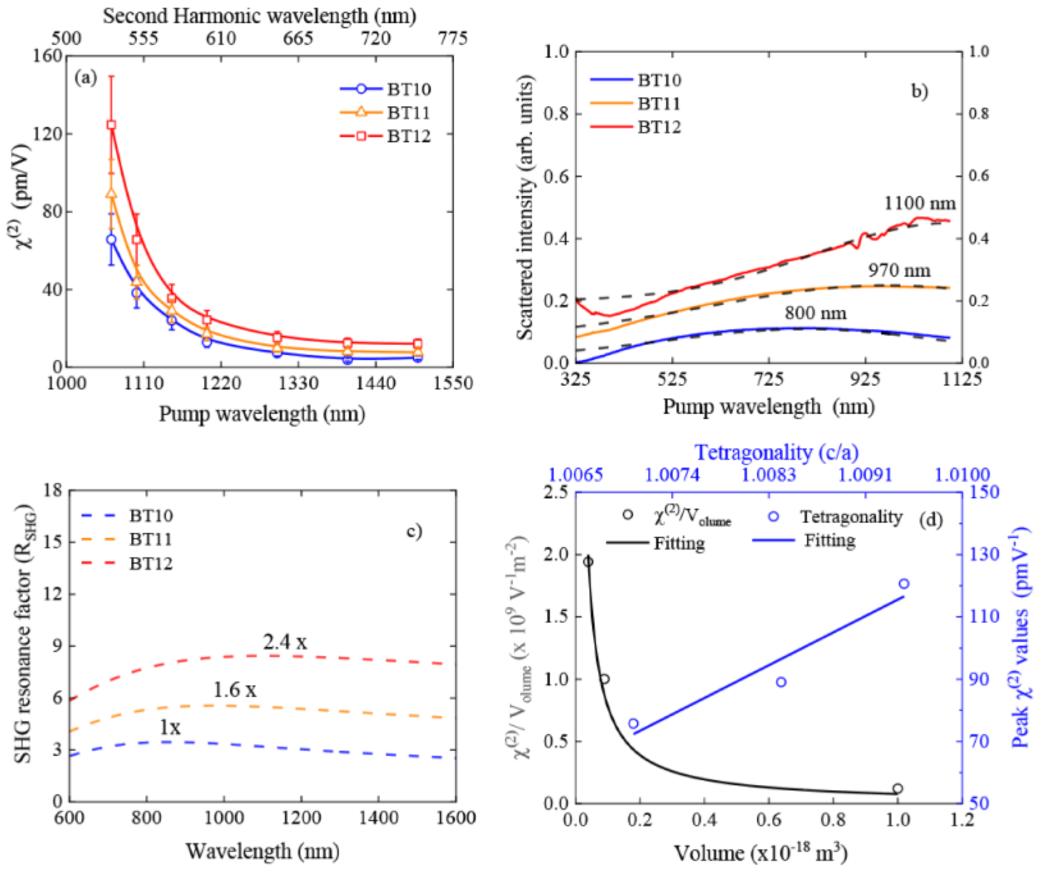

Figure 5. (a) Second-order nonlinear optical susceptibility dispersion values ($\chi^{(2)}$) for BT10, BT11, and BT12. (b) Linear Mie scattering spectra for BT10, BT11, and BT12. The black dashed line indicates the Gaussian decomposition, and the solid colored line displays the experimental results. (c) FOM of the SHG resonance factor $R_{(SHG)}$ as a function of incident wavelength. (d) Volume normalized peak $\chi^{(2)}$ values as a function of volume particle and as a function of tetragonality. $\chi^{(2)}$ and volume experimental errors are approximately 25% and 20%, respectively).

intracavity enhancement, which the Mie theory can describe.[47] Generally, the electric and magnetic dipoles and quadrupoles substantially contribute to the amplitude of Mie resonances that depend on the particle size, composition, and structural symmetry.[48] Considering this, Figure 5b displays the linear Mie scattering spectra of the studied samples.

Two main differences in the linear Mie scattering spectra related to varying sizes are the normalized intensity and shifts in peak positions. The peak positions for different particles are 800 nm (BT10), 970 nm (BT11), and 1100 nm (BT12), where the largest particle presents the greater scattered intensity. Therefore, to better understand the difference in peak SHG values, a figure of merit (FOM) was created. This FOM considers the amplitude of the scattered signal (A_{mie}), the frequency position of the maximum scattering (ω_{mie}), and the full width at half-maximum (fwhm) of the scattered spectra (Ω_{mie}). This parameter was called the SHG resonance factor (R_{SHG}) and is given by $R_{\mathrm{SHG}}(\omega) = \frac{A_{\mathrm{mie}}}{((\omega - \omega_{\mathrm{mie}})^2 + \Omega_{\mathrm{mie}}^2)}$. As observed in Figure 5c, at 1064 nm, the conversion efficiency of the SHG of the BT12 sample can be increased up to 2.4 times compared to the BT10 sample. It can be explained by the greater value of A_{mie} at the BT12 sample and the closer proximity to the Mie enhancement frequency (ω_{mie}). On the other hand, for wavelengths longer than Mie resonance, the contribution of the R_{SHG} factor remains approximately constant until the measured wavelengths result in different additional offsets in each sample.

Moreover, apart from the contribution of intracavity effects from Mie resonance, the geometric parameters such as tetragonality and volume can change substantially the second-order nonlinear optical response. The tetragonality in $BaTiO_3$ particles is connected to the displacement of O^{2-} ions relative to Ba^{2+} and Ti^{4+} ions, causing a network distortion. This effect is more pronounced in BT12, suggesting higher temperatures in BT12 yield stronger SHG efficiencies than those in BT10. The lattice distortion significantly affects the net dipole moments, inherently influencing the $\chi^{(2)}$. The Rietveld refinement demonstrated increased lattice parameters in the c-axis direction for BT12 relative to those for BT10. The net dipole moments for the unit cells have been quantified as approximately 1.9×10^{-31} C m for BT10, 2.3×10^{-31} C m for BT11, and 2.5×10^{-31} C m for BT12 along the c-axis direction. The increase in the c/a ratio in BT12, driven by an optimized Ti−O bond alignment along with the density of the TiO_6 octahedron, has a direct influence on the $\chi^{(2)}$ values.

As discussed, the increase in tetragonality, evidenced by the distortion of the $BaTiO_3$ lattice and the corresponding shifts in net dipole moments, suggests a profound impact on the material's nonlinear optical properties, particularly $\chi^{(2)}$. To quantitatively validate the relationship between tetragonality and $\chi^{(2)}$, we employed a Pearson correlation analysis across samples BT10, BT11, and BT12, where controlled adjustments in calcination temperatures varied tetragonality systematically. This quantitative approach allowed us to evaluate the strength and direction of the linear relationship between the tetragonality and $\chi^{(2)}$. The correlation coefficient, r, was calculated to be 0.89, indicating a strong positive correlation. This significant correlation underscores our hypothesis that enhanced tetragonality, which amplifies the noncentrosymmetry of the lattice, directly contributes to increased SHG efficiency. The strong correlation between increased tetragonality and enhanced $\chi^{(2)}$ values not only supports our physical observations of lattice distortion and electron distribution changes but also provides a robust quantitative framework for predicting SHG efficiencies based on structural properties. Furthermore, the observed wavelength dependence of $\chi^{(2)}$ due to Mie resonances elucidates how particle size variations modify the SHG efficiency, thereby providing detailed insights into the structural influences on the nonlinear optical behavior of $BaTiO_3$ nanoparticles.

The volume of the particle also emerges as a determinant factor in modulating the SHG signal. Studies concerning the $BaTiO_3$ nanoparticles showed that the total emitted power of SHG is proportional to the square of volume and second-order optical susceptibility.[49,50] Typically, larger volumes accommodate more unit cells, increasing the intensity of the signal up to specific thresholds. By our results, no variation is expected when $\chi^{(2)}$ values are normalized by the volume, in which $\frac{\chi^{(2)}}{\text{volume}} \propto C$, where C is constant. However, as shown in Figure 5d, a reciprocal function between the normalized volume peak $\chi^{(2)}$ values as a volume function was found at the measured range. The $\chi^{(2)}$ normalized volume analysis results in similar values for BT10 and BT11 but significantly lower values for BT12, indicating a considerable decrease in the efficiency conversion of SHG for the largest particle size. One possible explanation is associated with the loss of the fundamental and second harmonic (SH) light intensity given by the Mie scattering process. According to Jen and Gonella,[51] for polystyrene beads adsorbed with malachite green dye molecules in an aqueous solution, this loss can drop the SH conversion efficiency by up to 80%. This loss can be quantified through the Mie scattering loss coefficient (C_t),[51,52] which is exponentially proportional to the square of the particle size and the linear dependence of the optical path and linear scattering coefficients for the fundamental and SH light and the refraction index, where the linear scattering coefficients can be determined by Mie theory. Therefore, for the BT11 and BT12, compared to the BT10 sample, the SH conversion efficiency dropped 22% and 85%, respectively.

Understanding the influence of structural modifications and the enhancement mechanisms of SHG is essential, as is comprehending the origin of this frequency conversion in particles. Several theories explain the origin of SHG for particles. Beer et al.[53] and Gonella et al.[54] have highlighted that for particles larger than 200 nm, the interaction of light with particles deviates from the predictions of the Rayleigh−Gans−Debye approximation (particles lower than 200 nm).[52] Instead, such interactions are more aptly described by the nonlinear Mie theory,[54] which has pointed out that the SHG signal's intensity, $I(2\omega)$, is intrinsically tied to particle size, underscoring the significance of $\chi^{(2)}$ in this relationship. Chen et al.[55] stated that the significant SHG responses are attributed to the synergistic contribution of the octahedral distortion and the ordered arrangement in the noncentrosymmetric halide perovskite. Other authors showed the effect of micrometric particle size on variation in SHG intensity.[56,57] Additionally, the increase in electron−phonon coupling (section 3.2) modifies the electronic structure due to phonon vibrations. This alteration of the material's electronic structure can contribute to the $\chi^{(2)}$ values. For instance, Smitiukh et al.[58] have considered the electron−phonon effect on SHG intensity in powder particles as single crystals. Theoretical studies showed the influence on SHG and THG due to the electron−phonon interactions.[59,60] Thus, our results elucidate the dynamic interplay among particle size, lattice distortion, and electron−phonon coupling in determining the origin of the SHG intensity. This intricate interplay offers insights into potential pathways for material optimization aimed at enhancing nonlinear optical properties.

To address the applications of our enhanced SHG results, the increased $\chi^{(2)}$ of modified $BaTiO_3$ nanoparticles makes them candidates for bioimaging technologies, particularly for high-resolution, low-interference bioimaging. Demonstrating the highest $\chi^{(2)}$ among perovskite NLO particles like $LiNbO_3$, $PbTiO_3$, and others, our nanoparticles are ideal for nonlinear optical microscopy, which could offer high-contrast imaging through SHG and eliminate the need for external fluorescent labels.[3,14,61] This capability is advantageous for live-cell imaging and dynamic biological processes, where minimal perturbation is essential.[62] The improved SHG signal intensity observed in our research indicates that it can overcome current limitations in image quality and interpretation in biolabeling and bioimaging applications. Additionally, the correlation between enhanced tetragonality, controlled particle size, and SHG efficiency not only aligns with theoretical predictions noted in the literature but also reflects findings in similar nanoparticle systems used in optical diagnostics and therapeutic monitoring.[63,64]

4. CONCLUSION

This study provides insights into the intricate relationship between particle size, lattice distortion, and electron−phonon coupling in $BaTiO_3$ perovskite SHG. Employing Raman spectroscopy and X-ray Diffraction, we identified a systematic blueshift in Raman modes of $\Delta\omega = 15\ \text{cm}^{-1}$ and pronounced lattice strain due to thermal treatment. The figure of merit (FOM) explains an interesting relation between the size and the SHG enhancement, where the largest particles have a redshift wavelength at Mie resonances. The changes in tetragonality, characterized by shifts in the Ti−O bond length, correlated with net dipole moments ranging from 1.9×10^{-31} to 2.5×10^{-31} C m and also support the considerable variation in the $\chi^{(2)}$ values. A reciprocal relation between the normalized volume peak $\chi^{(2)}$ values and the volume function was found. The significant loss of conversion efficiency at the SH signal at the largest particles can be attributed to the Mie scattering process. Finally, these findings underscore the potential of $BaTiO_3$, serving as a roadmap for adjusting structural parameters in the development of optical and medical imaging applications.

■ AUTHOR INFORMATION

Corresponding Author

Cleber R. Mendonça − *São Carlos Institute of Physics, University of São Paulo, São Carlos, São Paulo 13560-970, Brazil;* orcid.org/0000-0001-6672-2186;
Email: crmendon@ifsc.usp.br

Authors

José L. Clabel Huamán − *São Carlos Institute of Physics, University of São Paulo, São Carlos, São Paulo 13560-970, Brazil;* orcid.org/0000-0002-7413-4795

Carlos H. D. Domingues dos Santos − *São Carlos Institute of Physics, University of São Paulo, São Carlos, São Paulo 13560-970, Brazil;* orcid.org/0000-0002-1255-2676

Leonardo De Boni − *São Carlos Institute of Physics, University of São Paulo, São Carlos, São Paulo 13560-970, Brazil;* orcid.org/0000-0002-1875-1852

Complete contact information is available at:
https://pubs.acs.org/10.1021/acs.jpcc.4c03049

Author Contributions

[#]J.L.C.H., C.H.D.D., L.D.B., and C.R.M. contributed equally.

Funding

The Article Processing Charge for the publication of this research was funded by the Coordination for the Improvement of Higher Education Personnel - CAPES (ROR identifier: 00x0ma614).

Notes

The authors declare no competing financial interest.

■ ACKNOWLEDGMENTS

The authors acknowledge financial support from the São Paulo Research Foundation (FAPESP) under the grants 2020/04835-3, 2018/11283-7, and 2021/11484-5; Conselho Nacional de Desenvolvimento Científico e Tecnológico (CNPq); Coordenação de Aperfeiçoamento de Pessoal de Nível Superior, Brasil (CAPES), Código de Financiamento 001; the Air Force Office of Scientific Research (AFOSR) (FA9550-23-1-0664); and the US Army (W911NF2110362).

■ REFERENCES

(1) Baranova, I. M.; Dolgova, T. V.; Kolmychek, I. A.; Maydykovskiy, A. I.; Mishina, E. D.; Murzina, T. V.; Fedyanin, A. A. Optical Second Harmonic Generation: Role of Symmetry and Local Resonances (Review). *Quantum Electron.* **2022**, *52*, 407−312.

(2) Yin, F.; Liu, L.; Zhu, M.; Lv, J.; Guan, X.; Zhang, J.; Lin, N.; Fu, X.; Jia, Z.; Tao, X. Transparent Lead-Free Ferroelectric (K, Na)NbO3 Single Crystal with Giant Second Harmonic Generation and Wide Mid-Infrared Transparency Window. *Adv. Opt. Mater.* **2022**, *10*, 2201721.

(3) Joulaud, C.; Mugnier, Y.; Djanta, G.; Dubled, M.; Marty, J.-C.; Galez, C.; Wolf, J.-P.; Bonacina, L.; Le Dantec, R. Characterization of the Nonlinear Optical Properties of Nanocrystals by Hyper Rayleigh Scattering. *J. Nanobiotechnol.* **2013**, *11*, 1−9.

(4) Clabel, H. J. L.; Zucolotto, L. H.; Pelosi, A. G.; de Queiroz Garcia, R.; Queiroz, R. G. D.; De Boni, L.; Mendonça, C. R. Nonlinear Optical Properties in Perovskite Structure and Their Applications. In *Metal-Halide Perovskite Semiconductors*; Nie, W.; Iniewski, K., Eds. Springer: Cham, 2023; Vol. *1*, pp. 185219.

(5) Clabel, H. J. L.; Baharuddin, N. A.; Mohamed, M. A.; Samat, A. A.; Abd Rahman, H.; Marega, E., Jr Recent Advances in Perovskite Ceramics: synthesis, Processing, and Applications. In *Advanced Ceramics - Advances in Material Research and Technology*, Ikhmayies, S. J., Eds. Springer Cham: 2023; Vol. *1*, pp. 47112.

(6) Ma, C.; Yan, J.; Wei, Y.; Liu, P.; Yang, G. Enhanced Second Harmonic Generation in Individual Barium Titanate Nanoparticles Driven by Mie Resonances. *J. Mater. Chem. C Mater.* **2017**, *5*, 4810−4819.

(7) Clabel, H. J. L.; Rivera, V. A. G. *Perovskite Ceramics: recent Advances and Emerging Applications*, 1st ed., Huaman, J. L. C.; Rivera, V. A. G., Eds. Elsevier, 2023, Vol. *1*.

(8) Senthilkumar, P.; Dhanuskodi, S.; Thomas, A. R.; Philip, R. Enhancement of Nonlinear Optical and Temperature Dependent Dielectric Properties of Ce: BaTiO3 Nano and Submicron Particles. *Mater. Res. Express* **2017**, *4*, 085027.

(9) Wang, Y.; Zhou, X. Y.; Chen, Z.; Cai, B.; Ye, Z. Z.; Gao, C. Y.; Huang, J. Y. Synthesis of Cubic LiNbO3 Nanoparticles and Their Application in Vitro Bioimaging. *Appl. Phys. A: mater. Sci. Process* **2014**, *117*, 2121−2126.

(10) Nakayama, Y.; Pauzauskie, P. J.; Radenovic, A.; Onorato, R. M.; Saykally, R. J.; Liphardt, J.; Yang, P. Tunable Nanowire Nonlinear Optical Probe. *Nature* **2007**, *447*, 1098−1101.

(11) Riporto, J.; Urbain, M.; Mugnier, Y.; Multian, V.; Riporto, F.; Bredillet, K.; Beauquis, S.; Galez, C.; Monnier, V.; Chevolot, Y.; et al. Second Harmonic Spectroscopy of ZnO, BiFeO3 and LiNbO3 Nanocrystals. *Opt. Mater. Express* **2019**, *9*, 1955.

(12) Kauranen, M.; Zayats, A. V. Nonlinear Plasmonics. *Nat. Photonics* **2012**, *6*, 737−748.

(13) Le Dantec, R.; Mugnier, Y.; Djanta, G.; Bonacina, L.; Extermann, J.; Badie, L.; Joulaud, C.; Gerrmann, M.; Rytz, D.; Wolf, J. P.; et al. Ensemble and Individual Characterization of the Nonlinear Optical Properties of ZnO and BaTiO3 Nanocrystals. *J. Phys. Chem. C* **2011**, *115*, 15140−15146.

(14) Barbosa-Silva, R.; Silva, J. F.; Rocha, U.; Jacinto, C.; de Araújo, C. B. Second-Order Nonlinearity of NaNbO3 Nanocrystals with Orthorhombic Crystalline Structure. *J. Lumin.* **2019**, *211*, 121−126.

(15) Butet, J.; Russier-Antoine, I.; Jonin, C.; Lascoux, N.; Benichou, E.; Brevet, P. F. Sensing with Multipolar Second Harmonic Generation from Spherical Metallic Nanoparticles. *Nano Lett.* **2012**, *12*, 1697−1701.

(16) Hsieh, C. L.; Grange, R.; Pu, Y.; Psaltis, D. Bioconjugation of Barium Titanate Nanocrystals with Immunoglobulin G Antibody for Second Harmonic Radiation Imaging Probes. *Biomaterials* **2010**, *31*, 2272−2277.

(17) Grange, R.; Lanvin, T.; Hsieh, C.-L.; Pu, Y.; Psaltis, D. Imaging with Second-Harmonic Radiation Probes in Living Tissue. *Biomed. Opt. Express* **2011**, *2*, 2532−2539.

(18) Staedler, D.; Magouroux, T.; Hadji, R.; Joulaud, C.; Extermann, J.; Schwung, S.; Passemard, S.; Kasparian, C.; Clarke, G.; Gerrmann, M.; et al. Harmonic Nanocrystals for Biolabeling: A Survey of Optical Properties and Biocompatibility. *ACS Nano* **2012**, *6*, 2542−2549.

(19) Clabel, H. J. L.; Sczancoski, J. C.; Marega, E.; Pinto, A. H. Methods for the Synthesis of Ceramic Materials with Perovskite Structure. In *Perovskite Ceramics: Recent Advances and Emerging Applications*; Clabel, H. J. L.; Rivera, V. A. G., Eds. Elservier, 2023; pp. 3175.

(20) Klinger, M.; Jäger, A. Crystallographic Tool Box (CrysTBox): Automated Tools for Transmission Electron Microscopists and Crystallographers. *J. Appl. Crystallogr.* **2015**, *48*, 2012−2018.

(21) Dos Santos, C. H. D.; Zucolotto, C. L. H.; Pelosi, A. G.; Batista, V. F.; Pinto, D. C. G. A.; Faustino, M. A. F.; Vivas, M. G.; de Paula Siqueira, J.; Mendonça, C. R.; De Boni, L. Observation of the Two-Photon Transition Enhanced First Hyperpolarizability Spectra in Cinnamaldehyde Derivatives: A Femtosecond Regime Study. *J. Chem. Phys.* **2023**, *158*, 214201.

(22) Clabel, H. J. L.; Awan, I. T.; Pinto, A. H.; Nogueira, I. C.; Bezzon, V. D. N.; Leite, E. R.; Balogh, D. T.; Mastelaro, V. R.; Ferreira, S. O.; Marega, E., Jr. Insights on the Mechanism of Solid State Reaction between TiO2 and BaCO3 to Produce BaTiO3 Powders: The Role of Calcination, Milling, and Mixing Solvent. *Ceram. Int.* **2020**, *46*, 2987−3001.

(23) Clabel, H. J. L.; Nicolodelli, G.; Lozano, G.; Rivera, V. A. G.; Ferreira, S. O.; Pinto, A. H.; Li, M. S.; Marega, E., Jr. The Extrinsic Nature of Double Broadband Photoluminescence from the BaTiO3 Perovskite: Generation of White Light Emitters. *Phys. Chem. Chem. Phys.* **2021**, *23*, 18694−18706.

(24) Buttner, R. H.; Maslen, E. N. Structural Parameters and Electron Difference Density in BaTiO3. *Acta Crystallogr. B* **1992**, *48*, 764−769.

(25) Hasbullah, N. N.; Chen, S. K.; Tan, K. B.; Talib, Z. A.; Liew, J. Y. C.; Lee, O. J. Photoluminescence Activity of BaTiO 3 Nanocubes via Facile Hydrothermal Synthesis. *J. Mater. Sci.: mater. Electron.* **2019**, *30*, 5149−5157.

(26) Buscaglia, V.; Randall, C. A. Size and Scaling Effects in Barium Titanate. An Overview. *J. Eur. Ceram. Soc.* **2020**, *40*, 3744−3758.

(27) Keswani, B. C.; Saraf, D.; Patil, S. I.; Kshirsagar, A.; James, A. R.; Kolekar, Y. D.; Ramana, C. V. Role of A-Site Ca and B-Site Zr Substitution in BaTiO3 Lead-Free Compounds: Combined Experimental and First Principles Density Functional Theoretical Studies. *J. Appl. Phys.* **2018**, *123*, 204104.

(28) Mukherjee, S.; Phuyal, D.; Segre, C. U.; Das, S.; Karis, O.; Edvinsson, T.; Rensmo, H. Structure and Electronic Effects from Mn and Nb Co-Doping for Low Band Gap BaTiO3Ferroelectrics. *J. Phys. Chem. C* **2021**, *125* (27), 14910−14923.

(29) Clabel, H. J. L.; Awan, I. T.; Rivera, V. A. G.; Nogueira, I. C.; Pereira-da-Silva, M. A.; Li, M. S.; Ferreira, S. O.; Marega, E. M. Growth Process and Grain Boundary Defects in Er Doped BaTiO3 Processed by EB-PVD: A Study by XRD, FTIR, SEM and AFM. *Appl. Surf. Sci.* **2019**, *493*, 982−993.

(30) Arshad, M.; Khan, W.; Abushad, M.; Nadeem, M.; Husain, S.; Ansari, A.; Chakradhary, V. K. Correlation between Structure, Dielectric and Multiferroic Properties of Lead Free Ni Modified BaTiO3 Solid Solution. *Ceram. Int.* **2020**, *46*, 27336−27351.

(31) Clabel, H. J. L.; Nazrin, S. N.; Lozano, C. G.; Pereira da Silva, M.; Siu Li, M.; Marega, E., Jr. Activation Energy and Its Fluctuations at Grain Boundaries of Er3+: BaTiO3 Perovskite Thin Films: Effect of Doping Concentration and Annealing Temperature. *Vacuum* **2021**, *194*, 110562.

(32) Amorín, H.; Jiménez, R.; Deluca, M.; Ricote, J.; Hungría, T.; Castro, A.; Algueró, M. Nanostructuring Effects in Piezoelectric BiScO 3- PbTiO3 Ceramics. *J. Am. Ceram. Soc.* **2014**, *97*, 2802−2809.

(33) Bianchi, U.; Kleemann, W.; Bednorz, J. G. Raman Scattering of Ferroelectric Sr 1-x Ca x TiO 3, X = 0.007. *J. Phys.: condens. Matter* **1994**, *6*, 1229.

(34) Spanier, J. E.; Robinson, R. D.; Zhang, F.; Chan, S. W.; Herman, I. P. Size-Dependent Properties of CeO2-d Nanoparticles as Studied by Raman Scattering. *Phys. Rev. B: condens. Matter Mater. Phys.* **2001**, *64*, 245407.

(35) Ouni, I. B.; Chapron, D.; Aroui, H.; Fontana, M. D. Ca Doping in BaTiO3 Crystal: Effect on the Raman Spectra and Vibrational Modes. *J. Appl. Phys.* **2017**, *121*, 114102.

(36) Chandramohan, P.; Srinivasan, M. P.; Velmurugan, S.; Narasimhan, S. V. Cation Distribution and Particle Size Effect on Raman Spectrum of CoFe2O4. *J. Solid State Chem.* **2011**, *184*, 89−96.

(37) Sati, A.; Kumar, A.; Mishra, V.; Warshi, K.; Pokhriyal, P.; Sagdeo, A.; Sagdeo, P. R. Temperature-Dependent Dielectric Loss in BaTiO3: Competition between Tunnelling Probability and Electron-Phonon Interaction. *Mater. Chem. Phys.* **2021**, *257*, 123792.

(38) Fano, U. Effects of Configuration Interaction on Intensities and Phase Shifts. *Phys. Rev.* **1961**, *124*, 1866−1878.

(39) Dwij, V.; De, B. K.; Tyagi, S.; Sharma, G.; Sathe, V. Fano Resonance and Relaxor Behavior in Pr Doped SrTiO3: A Raman Spectroscopic Investigation. *Physica B Condens. Matter* **2021**, *620*, 413265.

(40) Wu, Y.; Liang, F.; Wang, X.; Wang, J.; Yu, H.; Zhang, H. Temperature Dependent Raman Spectroscopic Study of Fano Resonance in Perovskite Ferroelectric KTa 1-x Nb x O 3 Single Crystal. *Opt. Mater. Express.* **2022**, *12*, 247.

(41) Sendova, M.; Hosterman, B. D. Raman Spectroscopic Study of the Size-Dependent Order Parameter of Barium Titanate. *J. Appl. Phys.* **2014**, *115*, 214104.

(42) Zhang, Y.; Tan, Y.; Dong, Y.; Dai, L.; Ren, C.; Zhang, F.; Zeng, L.; An, F.; Li, C.; Huang, B.; et al. High-Throughput Scanning Second-Harmonic-Generation Microscopy for Polar Materials. *Adv. Mater.* **2023**, *35*, 2300348.

(43) Madzharova, F.; Nodar, Á.; Živanović, V.; Huang, M. R. S.; Koch, C. T.; Esteban, R.; Aizpurua, J.; Kneipp, J. Gold- and Silver-Coated Barium Titanate Nanocomposites as Probes for Two-Photon Multimodal Microspectroscopy. *Adv. Funct. Mater.* **2019**, *29*, 1904289.

(44) Kim, E.; Steinbru, A.; Buscaglia, M. T.; Buscaglia, V.; Pertsch, T.; Grange, R. Second-Harmonic Generation of Single BaTiO3 Nanoparticles down to 22 Nm Diameter. *ACS Nano* **2013**, *7*, 5343−5349.

(45) Roke, S.; Gonella, G. Nonlinear Light Scattering and Spectroscopy of Particles and Droplets in Liquids. *Annu. Rev. Phys. Chem.* **2012**, *63*, 353−378.

(46) Timpu, F.; Sergeyev, A.; Hendricks, N. R.; Grange, R. Second-Harmonic Enhancement with Mie Resonances in Perovskite Nanoparticles. *ACS Photonics* **2017**, *4*, 76−84.

(47) Craig, F. B.; Donald, R. H. *Absorption and Scattering of Light by Small Particles*, 1st ed.; Craig, F. B.; Donald, R. H., Eds. WILEY-VCH Verlag GmbH & Co: New York, 1998.

(48) Smirnova, D.; Smirnov, A. I.; Kivshar, Y. S. Multipolar Second-Harmonic Generation by Mie-Resonant Dielectric Nanoparticles. *Phys. Rev. A* **2018**, *97*, 013807.

(49) Hsieh, C.; Grange, R.; Pu, Y.; Psaltis, D. Three-Dimensional Harmonic Holographic Microcopy Using Nanoparticles as Probes for Cell Imaging. *Opt. Express.* **2009**, *17*, 2880−2891.

(50) Kim, E.; Steinbrück, A.; Buscaglia, M. T.; Buscaglia, V.; Pertsch, T.; Grange, R. Second-Harmonic Generation of Single BaTiO3 Nanoparticles down to 22 Nm Diameter. *ACS Nano* **2013**, *7*, 5343−5349.

(51) Jen, S. H.; Gonella, G.; Dai, H. L. The Effect of Particle Size in Second Harmonic Generation from the Surface of Spherical Colloidal Particles. i: Experimental Observations. *J. Phys. Chem. A* **2009**, *113*, 4758−4762.

(52) Jen, S. H.; Dai, H. L.; Gonella, G. The Effect of Particle Size in Second Harmonic Generation from the Surface of Spherical Colloidal Particles. II: The Nonlinear Rayleigh-Gans-Debye Model. *J. Phys. Chem. C* **2010**, *114*, 4302−4308.

(53) De Beer, A. G. F.; Roke, S. Nonlinear Mie Theory for Second-Harmonic and Sum-Frequency Scattering. *Phys. Rev. B: condens. Matter Mater. Phys.* **2009**, *79*, 155420.

(54) Gonella, G.; Dai, H. L. Determination of Adsorption Geometry on Spherical Particles from Nonlinear Mie Theory Analysis of Surface Second Harmonic Generation. *Phys. Rev. B: condens. Matter Mater. Phys.* **2011**, *84*, 121402.

(55) Chen, D.; Hao, S.; Fan, L.; Guo, Y.; Yao, J.; Wolverton, C.; Kanatzidis, M. G.; Zhao, J.; Liu, Q. Broad Photoluminescence and Second-Harmonic Generation in the Noncentrosymmetric Organic-Inorganic Hybrid Halide (C6H5(CH2)4NH3)4MX7·H2O (M = Bi, In, X = Br or I). *Chem. Mater.* **2021**, *33*, 8106−8111.

(56) Cao, J.; Liu, K.; Quan, M.; Hou, A.; Jiang, X.; Lin, Z.; Zhao, J.; Liu, Q. Second Harmonic Generation from Symmetry Breaking Stimulated by Mixed Organic Cations in Zero-Dimensional Hybrid Metal Halides. *Dalton Trans.* **2023**, *52*, 9368−9376.

(57) Wang, J.; Butet, J.; Baudrion, A. L.; Horrer, A.; Lévêque, G.; Martin, O. J. F.; Meixner, A. J.; Fleischer, M.; Adam, P. M.; Horneber, A.; et al. Direct Comparison of Second Harmonic Generation and Two-Photon Photoluminescence from Single Connected Gold Nanodimers. *J. Phys. Chem. C* **2016**, *120*, 17699−17710.

(58) Smitiukh, O. V.; Marchuk, O. V.; Kogut, Y. M.; Yukhymchuk, V. O.; Mazur, N. V.; Myronchuk, G. L.; Ponedelnyk, S. M.; Cherniushok, O. I.; Parashchuk, T. O.; Khyzhun, O. Y.; et al. Effect of Rare-Earth Doping on the Structural and Optical Properties of the Ag3AsS3 Crystals. *Opt. Mater. Express.* **2022**, *54*, 224.

(59) Khordad, R.; Bahramiyan, H. The Second and Third-Harmonic Generation of Modified Gaussian Quantum Dots under Influence of Polaron Effects. *Superlattices Microstruct.* **2014**, *76*, 163−173.

(60) Hashemi, P.; Servatkhah, M.; Pourmand, R. Influence of Polaron on Second and Third Harmonic Generation of Tuned Quantum Dot/Ring Systems. *Opt. Commun.* **2022**, *506*, 127551.

(61) Rodriguez, E. V.; Araújo, C. B. D.; Brito-Silva, A. M.; Ivanenko, V. I.; Lipovskii, A. A. Hyper-Rayleigh Scattering from BaTiO3 and PbTiO3 Nanocrystals. *Chem. Phys. Lett.* **2009**, *467*, 335−338.

https://doi.org/10.1021/acs.jpcc.4c03049

(62) Sugiyama, N.; Sonay, A. Y.; Tussiwand, R.; Cohen, B. E.; Pantazis, P. Effective Labeling of Primary Somatic Stem Cells with BaTiO3 Nanocrystals for Second Harmonic Generation Imaging. *Small* **2018**, *14*, 1703386.

(63) Wang, W.; Li, J.; Liu, H.; Ge, S. Advancing Versatile Ferroelectric Materials Toward Biomedical Applications. *Adv. Sci.* **2021**, *8*, 2003074.

(64) Gheata, A.; Gaulier, G.; Campargue, G.; Vuilleumier, J.; Kaiser, S.; Gautschi, I.; Riporto, F.; Beauquis, S.; Staedler, D.; Diviani, D.; et al. Photoresponsive Nanocarriers Based on Lithium Niobate Nanoparticles for Harmonic Imaging and On-Demand Release of Anticancer Chemotherapeutics. *ACS Nanosci. Au* **2022**, *2*, 355−366.